

Jonathan B. Hopkins^{1,2}

Mechanical and Aerospace Engineering,
University of California, Los Angeles,
420 Westwood Plaza,
46-147F Engineering IV. Bldg.,
Los Angeles, CA 90095
e-mail: hopkins@seas.ucla.edu;
jonathanbhopskins@gmail.com

Jordan Rivera¹

Mechanical Engineering,
Bucknell University,
701 Moore Ave.,
Lewisburg, PA 17837
e-mail: jar055@bucknell.edu

Charles Kim

Mechanical Engineering,
Bucknell University,
701 Moore Ave.,
Lewisburg, PA 17837
e-mail: charles.kim@bucknell.edu

Girish Krishnan

Industrial and Enterprise Systems Engineering,
Illinois at Urbana-Champaign,
314 Transportation Bldg. 104 S. Mathews,
Urbana, IL 61801
e-mail: gkrishna@illinois.edu

Synthesis and Analysis of Soft Parallel Robots Comprised of Active Constraints

In this paper, we introduce a new type of spatial parallel robot that is comprised of soft inflatable constraints called trichamber actuators (TCAs). We extend the principles of the freedom and constraint topologies (FACT) synthesis approach to enable the synthesis and analysis of this new type of soft robot. The concepts of passive and active freedom spaces are introduced and applied to the design of general parallel systems that consist of active constraints (i.e., constraint that can be actuated to impart various loads onto the system's stage) that both drive desired motions and guide the system's desired degrees of freedom (DOFs). We provide the fabrication details of the TCA constraints introduced in this paper and experimentally determine their appropriate FACT-based constraint model. We fabricate a soft parallel robot that consists of three TCA constraints and verify and validate its FACT-predicted performance using finite element analysis (FEA) and experimental data. Other such soft robots are synthesized using FACT as case studies. [DOI: 10.1115/1.4029324]

Keywords: freedom and constraint topologies, FACT, soft-robots, passive and active freedom space, active constraints, soft actuators, parallel mechanisms

1 Introduction

Soft robotics has grown steadily in recent years [1]. There has been increasing interest in the use of unconventional soft materials and morphologies in robotic systems because of the unique advantages they provide in terms of motion and structure [2]. Soft robots open a larger range of possibilities beyond the constraints of rigid robotic systems. While a traditional "hard robot" typically has each kinematic degree of freedom controlled by actuation, soft robots have distributed deformation, which allows components to function as both constraints and actuation simultaneously [3].

Soft robots typically exhibit passive DOFs that give rise to unique conformal behavior. Most soft robots can utilize passive compliance to attain highly articulated motion or other kinematic functionality that would be difficult to attain with rigid systems. The tradeoff in obtaining this unique behavior is that analysis and control becomes significantly more challenging. Highly flexible bodies are inherently more difficult to analyze due to the nonlinear material properties and large deformation. Control is also limited by both dynamic bandwidth and sensing fidelity.

Systems such as walkers [4] and highly articulated continuum arms [5] have taken advantage of the compliance of silicone rubbers and/or pneumatic actuators to create dramatic motions and novel locomotion. Harvard's planar quadruped walker [4] uses channeled pneumatics to direct expansion of particular sections of the body in order to generate bending in the limbs. By

coordinating the individual limbs simple walking motions can be achieved. More complex motions require a more complex system of actuation and coordination of actuators. The OctArm continuum manipulator [5] uses combined arrays of extending pneumatic actuators to develop motions. By joining concentric sets of three or six contracting air muscles with rigid plates at both ends, OctArm accomplishes significant bending motions.

By modifying the geometry of fiber windings on inflatable membranes, complex motions have been obtained from limited channels of pressure [6]. Fiber reinforced elastomeric enclosures (FREEs) utilize specific fiber winding to create motions such as bending, twisting, and helical motion. Similar to FREEs, a generalized deformable cylindrical actuator with mechanical constraints imposed to orient the overall motion has been investigated [7]. By combining these actuators in parallel bundles, multiple motions can be combined to make new distinct ones [8].

The focus of this paper is to introduce a systematic approach for analyzing and synthesizing soft robots comprised of spatial parallel arrangements of TCAs (Fig. 1). In their current embodiment, TCAs are silicone cylinders with three internal axial cavities that can be inflated using pressurized fluids. Inflating one or two chambers causes bending and inflating all three chambers causes axial stretching.

Suzumori [9] laid the groundwork for inflatable TCAs in his research on the flexible micro-actuator (FMA). The FMA has a nearly identical architecture to the TCA except that the FMA is significantly smaller and utilizes wedge-shaped cross sections instead of circular cross sections to form the actuator's internal cavities. Suzumori and his colleagues have continued research utilizing FMAs for more than 20 years, but most of that research has focused on individual actuators or combinations of these actuators in series [10]. Similar to the premise of OctArm, linking the

¹These are co-first authors due to their equal level of contribution to this paper.

²Corresponding author.

Contributed by the Mechanisms and Robotics Committee of ASME for publication in the JOURNAL OF MECHANISMS AND ROBOTICS. Manuscript received September 24, 2014; final manuscript received December 2, 2014; published online December 31, 2014. Assoc. Editor: Carl Nelson.

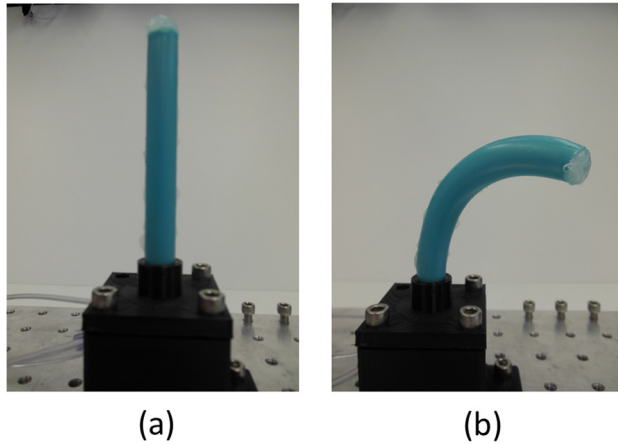


Fig. 1 TCA. Inflation of combinations of three internal chambers leads to extension (a) or bending (b).

actuators in series provides an increase in the DOFs. Indeed, this mechanism architecture has enabled the design of simple grippers and novel systems for controlling a small camera [9].

One problem in combining the actuators in a serial architecture, however, is that it compromises load-bearing capacity. The fundamental issue in combining long and thin actuators in series is that passive bending stiffness dominates the deformation behavior. The addition of any external loading can exceed the ability of these TCAs to support loads.

In this paper, we seek to enhance overall system stiffness and load-bearing capacity by utilizing spatial parallel arrangements of TCAs in a way that maintains desired mobility. A parallel system using TCAs can take on a number of different forms. We focus on parallel systems consisting of a single rigid stage connected directly to a fixed ground by TCAs (Fig. 2). Whereas most flexure-based stages of similar topologies consist of completely passive elements, the TCAs provide both structural constraint and actuator load. We call such elements active constraints.

Although over a century of significant research effort has focused on the kinematic design of parallel mechanisms [11,12], a fundamental part of this research is to develop new systematic methods by which systems comprised of active constraints can be

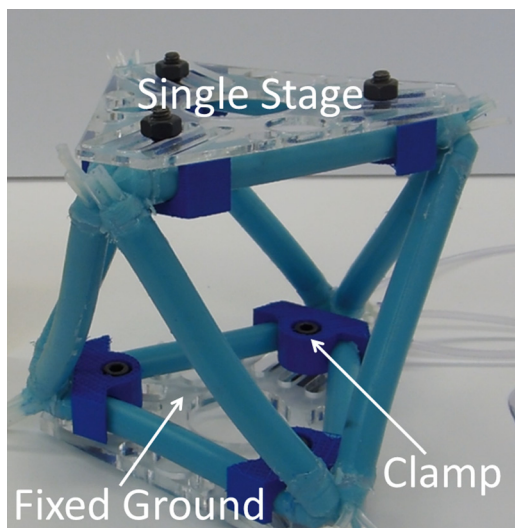


Fig. 2 Parallel system consisting of inflatable TCAs

designed and analyzed. To that end, we apply the principles of the FACT synthesis approach [13,14] to the analysis and design of such soft robots. At its core, the FACT approach provides designers with a comprehensive library of intuitive, geometric shapes that represent the mathematics of screw theory [15,16]. These shapes have traditionally been used to help designers visualize and consider all the ways a system may be passively constrained to achieve the system's desired DOFs. We review the fundamentals of FACT in Sec. 2.

In Sec. 3, we extend the principles of FACT such that designers may use the same geometric shapes to analyze parallel systems that possess wirelike active constraints that both constrain and actuate the system. We introduce and distinguish between the concepts of passive freedom space (PFS) and active freedom space (AFS) and provide the mathematics necessary to calculate both spaces. We initially apply these concepts to parallel systems that possess active constraints that are only capable of imparting pure forces along their axes. We later extend these principles to the analysis of parallel systems that consist of active constraints that can impart any type and number of loads onto the stage that they constrain. We provide the mathematics necessary to calculate the output load magnitude ratios of any general parallel system for driving its stage with any desired motion within the system's AFS. In Sec. 4, systematic steps are established for synthesizing parallel systems that possess wirelike active constraints that can only impart pure forces along their axes and can achieve any desired set of actuated motions. Two example case studies are synthesized using these steps. The paper's principles are then applied to the synthesis and analysis of soft parallel robots that consist of TCAs. In Sec. 5, we experimentally demonstrate that TCAs passively behave as wire flexure constraints and we experimentally determine the effective material properties for any general TCA. In Sec. 6, two soft parallel robots made of TCAs are built, analyzed, and tested using the principles discussed previously. FEA and experimental data are used to verify and validate the FACT-predicted behavior of one of these robots. Note that the theory provided in this paper is limited to small motion deformations and is subject to the approximations of linear analysis.

2 Fundamental Principles of FACT

This section reviews the fundamental principles of the FACT approach that are necessary to enable the analysis and synthesis of new parallel systems that consist of active constraints.

According to screw theory, all motions may be modeled using 6×1 twist vectors, \mathbf{T} , defined in Refs. [14–16]. Traditionally, twist vectors represent instantaneous velocities. For the purposes of this paper, however, we will assume that all the twist vectors discussed have been multiplied by a small time interval such that they represent small displacements instead. Moreover, twist vectors that model rotational motions in this paper are depicted as red lines about which the system's stage rotates, twist vectors that model translational motions are depicted as black arrows that point in the directions along which the system's stage translates, and twist vectors that model screw motions are depicted as green lines along and about which the system's stage simultaneously translates and rotates with a specific pitch. Consider, for instance, the 3DOFs of the parallel system shown in Fig. 3(a). The system's three wire flexure constraints permit its stage to move with two translations, modeled by \mathbf{T}_1 and \mathbf{T}_2 , and one rotation, modeled by \mathbf{T}_3 . These three motions are not the only motions the system's constraints permit. The system's stage may also move with every combination of these three motions. Such motions may be depicted as the infinitely large box of parallel red rotation lines, and the disk of perpendicular black translation arrows shown on the left side of Fig. 3(b). These geometric shapes constitute the system's freedom space [13,14]. A system's freedom space represents every permissible motion the system may achieve. The

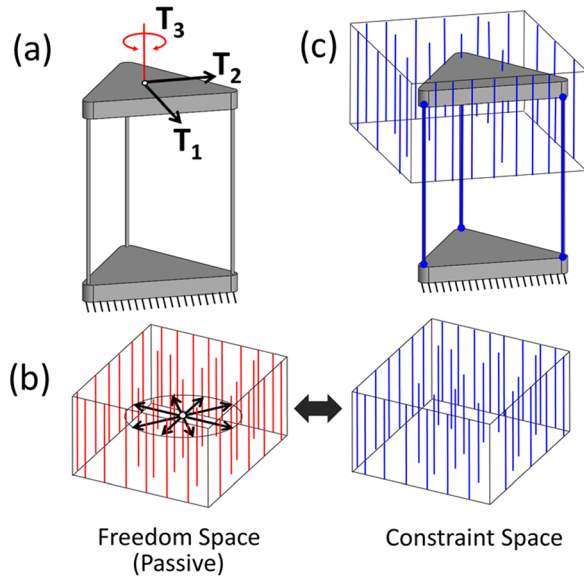


Fig. 3 Desired DOFs (a), freedom and constraint spaces (b), and constraints lie within the space (c)

number of independent twist vectors within the space, n , is the number of DOFs the system possesses. For example, in Fig. 3, n is 3.

Every freedom space uniquely links to a complementary constraint space [13,14]. The constraint space of the freedom space, shown in Fig. 3(b), is an infinitely large box of parallel constraint lines that are parallel with the rotation lines of the freedom space. Constraint lines, which are shown as blue lines in this paper, represent the axes of constraints that are only capable of imparting forces along their axis, like the wire flexures shown in Fig. 3(a). Thus, a system's constraint space is a geometric shape that represents the region from which constraints can be selected that enable the motions of its freedom space. Note, therefore, that the axes of the system's wire flexures all lie within the system's constraint space as shown in Fig. 3(c). The blue constraint lines within a constraint space may be modeled using 6×1 wrench vectors, \mathbf{W} , defined in Refs. [14–16]. If a system's freedom space contains n independent twist vectors (i.e., DOFs), its complementary constraint space consists of m independent wrench vectors according to

$$6 - n = m \quad (1)$$

Thus, designers must not only select constraints from within the system's constraint space to achieve the desired DOFs of its freedom space but also select m independent constraints (i.e., non-redundant constraints) from within that constraint space if the system is to achieve the n desired DOFs with no extra ones. The issue of how to select constraints within a constraint space such that they are independent is not the focus of this paper but is addressed in detail in Ref. [14]. If additional constraints are selected from the constraint space of a system that is already constrained by m nonredundant constraints, the system will possess redundant constraints (i.e., dependent wrench vectors) and is said to be overconstrained. Note that the system in Fig. 3(c) possesses three independent wire flexures and is thus not overconstrained because both n and m equal three and these numbers satisfy Eq. (1). Such parallel systems are exactly constrained (i.e., not overconstrained).

The FACT approach is comprehensive in that it consists of a finite body of freedom and constraint space pairs called types and

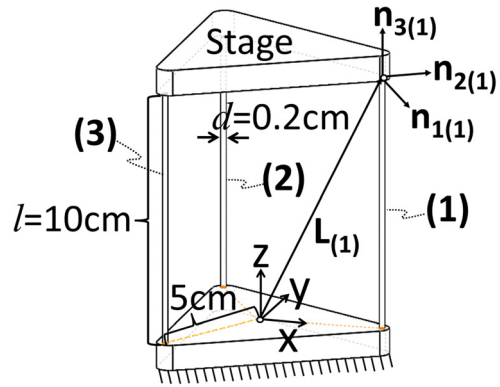


Fig. 4 Parameters necessary to define the system's twist-wrench stiffness matrix

all of these types are provided and described in detail in Ref. [17]. With this comprehensive body of types, designers may rapidly consider and compare every design concept that achieves any desired set of DOFs before selecting the final concept that best satisfies the desired design requirements. According to the convention provided in Ref. [17], the freedom and constraint space pair or type shown in Fig. 3(b) is 3DOF Type 2.

Once the shapes of FACT have been properly utilized to synthesize the topology of a parallel system that achieves a desired set of DOFs, designers can analytically construct a twist-wrench stiffness matrix [17–19] to analyze the system's quasi-static response to any actuation load. We now review the principles necessary to construct this stiffness matrix for a general parallel system constrained by cylindrical wire flexures like the system shown in Fig. 3. We will use this system, shown again in Fig. 4, as an example case study for this section.

To find the twist-wrench stiffness matrix, $[K_{TW}]$, of the parallel system in Fig. 4, we must first calculate the stiffness matrix of each wire flexure individually. The stiffness matrix of the first wire flexure labeled (1) in Fig. 4, $[K_{(1)}]$, is

$$[K_{(1)}] = [N_{(1)}][\Delta][S_{(1)}][N_{(1)}]^{-1} \quad (2)$$

where $[N_{(1)}]$ is a 6×6 matrix defined by

$$[N_{(1)}] = \begin{bmatrix} \mathbf{n}_{1(1)} & \mathbf{n}_{2(1)} & \mathbf{n}_{3(1)} & \mathbf{0} & \mathbf{0} & \mathbf{0} \\ \mathbf{L}_{(1)} \times \mathbf{n}_{1(1)} & \mathbf{L}_{(1)} \times \mathbf{n}_{2(1)} & \mathbf{L}_{(1)} \times \mathbf{n}_{3(1)} & \mathbf{n}_{1(1)} & \mathbf{n}_{2(1)} & \mathbf{n}_{3(1)} \end{bmatrix} \quad (3)$$

and $\mathbf{n}_{1(1)}$, $\mathbf{n}_{2(1)}$, and $\mathbf{n}_{3(1)}$ are 3×1 orthogonal unit vectors, $\mathbf{0}$ is a 3×1 vector of zeroes, and $\mathbf{L}_{(1)}$ is a 3×1 vector that points from the global coordinate system to the central point where the wire labeled (1) attaches to the system's stage as shown in Fig. 4. Note that $\mathbf{n}_{3(1)}$ must point into the stage along the wire's axis. The directions of $\mathbf{n}_{1(1)}$ and $\mathbf{n}_{2(1)}$ are somewhat arbitrary because the constraint labeled (1) in Fig. 4 is an axisymmetric cylindrical wire flexure. These two unit vectors must, however, be perpendicular to the wire's axis and be orthogonal with respect to each other as well. The 6×6 matrix $[\Delta]$ in Eq. (2) is defined by

$$[\Delta] = \begin{bmatrix} [0_{3 \times 3}] & [I_{3 \times 3}] \\ [I_{3 \times 3}] & [0_{3 \times 3}] \end{bmatrix} \quad (4)$$

where $[0_{3 \times 3}]$ is a 3×3 matrix of zeroes and $[I_{3 \times 3}]$ is a 3×3 identity matrix. As long as the wire labeled (1) is long and slender such that it can be modeled using Euler–Bernoulli equations, the 6×6 $[S_{(1)}]$ matrix in Eq. (2) is defined by

$$[S_{(1)}] = \begin{bmatrix} \frac{l_{(1)}}{E_{(1)}I_{1(1)}} & 0 & 0 & 0 & -\frac{l_{(1)}^2}{2E_{(1)}I_{1(1)}} & 0 \\ 0 & \frac{l_{(1)}}{E_{(1)}I_{2(1)}} & 0 & \frac{l_{(1)}^2}{2E_{(1)}I_{2(1)}} & 0 & 0 \\ 0 & 0 & \frac{l_{(1)}}{G_{(1)}J_{3(1)}} & 0 & 0 & 0 \\ 0 & \frac{l_{(1)}^2}{2E_{(1)}I_{2(1)}} & 0 & \frac{l_{(1)}^3}{3E_{(1)}I_{2(1)}} & 0 & 0 \\ -\frac{l_{(1)}^2}{2E_{(1)}I_{1(1)}} & 0 & 0 & 0 & \frac{l_{(1)}^3}{3E_{(1)}I_{1(1)}} & 0 \\ 0 & 0 & 0 & 0 & 0 & \frac{l_{(1)}}{E_{(1)}A_{(1)}} \end{bmatrix}^{-1} \quad (5)$$

where $l_{(1)}$ is the length of the wire labeled (1) in Fig. 4, $E_{(1)}$ is this wire's Young's Modulus, $G_{(1)}$ is its shear modulus, $I_{1(1)}$ and $I_{2(1)}$ are the wire's second moments of inertia about the axes defined by the directions $\mathbf{n}_{1(1)}$ and $\mathbf{n}_{2(1)}$, respectively, $J_{3(1)}$ is the wire's polar moment of inertia about the axis defined by the direction $\mathbf{n}_{3(1)}$, and $A_{(1)}$ is the wire's cross-sectional area. These values are defined with respect to the wire's diameter, d , as

$$I_{1(1)} = I_{2(1)} = \frac{d^4\pi}{64} \quad (6)$$

$$J_{3(1)} = \frac{d^4\pi}{32} \quad (7)$$

and

$$A_{(1)} = \frac{d^2\pi}{4} \quad (8)$$

The entire parallel system's twist-wrench stiffness matrix, $[K_{TW}]$, can then be calculated by calculating each wire's stiffness matrix, $[K_{(i)}]$, individually using Eq. (2), and then sum them together according to

$$[K_{TW}] = \sum_{i=1}^C [K_{(i)}] \quad (9)$$

where C is the number of wire flexure constraints in the parallel system. For example, in Fig. 4, C is 3.

3 Passive Verses AFSs

This section introduces the concepts of passive versus AFSs. It also extends the principles reviewed in Sec. 2 to enable the generation of such spaces applied to general parallel systems constrained by active wirelike constraints. Active constraints are constraints that both constrain the system and also drive or actuate the system by imparting forces or moments to the system's stage. An example of an active constraint would be a wire flexure made of piezo-electric material. Such a constraint would not only guide the desired DOFs of the system but it could also extend and contract along its axis to drive the system's stage with other motions (that are not the system's DOFs) when subjected to a change in voltage.

To determine the motions that result from driving an active constraint within a general parallel system, we will consider again the system in Fig. 4. Suppose all of the constraints within this system are made of a material with a Young's Modulus, E , of 68 GPa and a shear modulus, G , of 25 GPa. Suppose also that the system's wire flexures possess the geometric dimensions specified in Fig. 4. If we allow the wire flexure labeled (1) in Fig. 4 to impart a pure

force wrench vector load, $\mathbf{W}_{(1)}$, on the system's stage as shown by the blue arrow in Fig. 5(a), we can calculate the resulting twist vector motion of the stage, $\mathbf{T}_{(1)}$ according to

$$\mathbf{T}_{(1)} = ([K_{TW}] - [K_{(1)}])^{-1} f_{(1)} \mathbf{W}_{(1)} \quad (10)$$

where $[K_{TW}]$ is the system's twist-wrench stiffness matrix defined in Eq. (9), $[K_{(i)}]$ is the stiffness matrix of the wire constraint labeled (1) in Fig. 4 (defined in Eq. (2)), $f_{(1)}$ is the scalar magnitude of the load imparted to the stage by this wire when it is actuated, and $\mathbf{W}_{(1)}$ is a 6×1 wrench vector with a force magnitude of unity defined by

$$\mathbf{W}_{(1)} = \begin{bmatrix} \mathbf{u}_{(1)} \\ \mathbf{L}_{(1)} \times \mathbf{u}_{(1)} + q_{(1)}\mathbf{u}_{(1)} \end{bmatrix} \quad (11)$$

where $\mathbf{u}_{(1)}$ is a 3×1 unit vector that points in the direction of the load, $\mathbf{L}_{(1)}$ is the 3×1 location vector shown in Fig. 4 that points from the coordinate system to the location where the wire constraint labeled (1) attaches to the system's stage, and $q_{(1)}$ is a scalar value that represents the wrench's moment to force ratio. For an active wire constraint that can only impart a pure force along its axis (shown as the blue arrow in Fig. 5(a)), $q_{(1)}$ is zero and $\mathbf{u}_{(1)}$ points in the direction of $\mathbf{n}_{3(1)}$ shown in Fig. 4 (i.e., it points along the wire's axis into the stage). By applying Eq. (10) to the system of Fig. 4, we can calculate the twist vector $\mathbf{T}_{(1)}$ that results when the active constraint labeled (1) imparts a pure force wrench vector, $\mathbf{W}_{(1)}$, with a magnitude of $f_{(1)}$ along the wire's axis onto the system's stage. We find that the stage rotates about the red line shown in Fig. 5(a) with a rotational magnitude, which can be calculated by decomposing the resulting twist vector $\mathbf{T}_{(1)}$. This rotational magnitude is dependent on the value of $f_{(1)}$, but the location and orientation of the twist vector's rotational axis are not. Note from Fig. 5(a) that this resulting rotational axis intersects and is half way down the length of the wire flexures labeled (2) and (3).

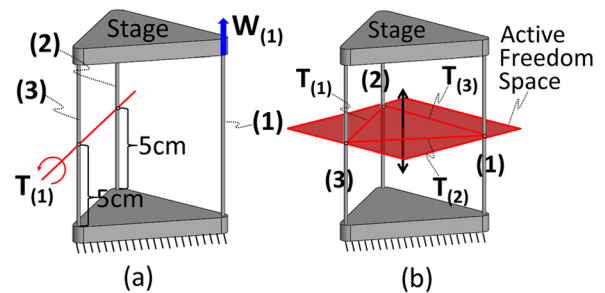


Fig. 5 Resulting twist produced by actuating wire (1) (a), system's AFS (b)

To find every possible way, the stage could move if all three active wire constraints could simultaneously impart pure forces along their axes with independent magnitudes, we must first calculate all the twist vectors, $\mathbf{T}_{(i)}$, that result from actuating their corresponding wire constraints with a wrench vector $\mathbf{W}_{(i)}$ that has a load magnitude $f_{(i)}$ of unity. We must then place these twist vectors in a matrix, $[\mathbf{T}_{\text{AFS}}]$, according to

$$[\mathbf{T}_{\text{AFS}}] = [\mathbf{T}_{(1)} \quad \mathbf{T}_{(2)} \quad \cdots \quad \mathbf{T}_{(C)}] \quad (12)$$

where

$$\mathbf{T}_{(i)} = ([K_{\text{TW}}] - [K_{(i)}])^{-1} \mathbf{W}_{(i)} \quad (13)$$

and C is the number of active constraints in the system. For the system of Fig. 5, C is 3. All three of the system's resulting twist vectors, $\mathbf{T}_{(1)}$, $\mathbf{T}_{(2)}$, and $\mathbf{T}_{(3)}$ (one from each active constraint), are shown as red rotation lines in Fig. 5(b). Finally, if we linearly combine these twist vectors according to

$$\mathbf{T}_{\text{AFS}} = [\mathbf{T}_{\text{AFS}}] \cdot [f_{(1)} \quad f_{(2)} \quad \cdots \quad f_{(C)}]^T \quad (14)$$

and allow their corresponding load magnitudes, $f_{(i)}$, to be any real and finite value, we produce a twist vector, \mathbf{T}_{AFS} , that represents every possible stage motion that can be achieved by actuating all C active constraints. For the system of Fig. 5, every resulting \mathbf{T}_{AFS} vector is either a rotation line that lies on a plane that is half way down the length of the wire constraints shown by the red plane in Fig. 5(b), or a black translation arrow that is perpendicular to this plane. This planar geometric shape is the system's AFS. *A system's AFS is a geometric shape that represents all the stage motions that can be achieved by actuating the system's active constraints. A system's PFS is a geometric shape that represents all the stage's motions that are permitted (i.e., not constrained) by the system's constraints when they are not being actuated (i.e., behaving as passive constraints).* A system's PFS is the linearly combination of its DOFs and is synonymous with the traditional definition of a freedom space. Thus, the PFS of the system in Fig. 5 is the freedom space shown in Fig. 3(b).

For parallel systems consisting of wirelike constraints that are all active in that they can each only impart a single pure force load along their axes, the system's AFS will possess the same number of independent twist vectors as there are independent wrench vectors within the complementary constraint space of the system's PFS (i.e., m). Thus, this number, in conjunction with the number of independent twist vectors within the system's PFS (i.e., n), satisfies Eq. (1). It is also significant to note that the independent twist vectors within the PFS of such a system are independent from the independent twist vectors within the system's AFS. Thus, the twist vectors within the system's PFS combined with the twist vectors within the same system's AFS result in the 6DOF Type 1 freedom space from the FACT library [17]. This freedom space possesses six independent twists and represents every possible motion. We will use these principles in Sec. 4 to help designers synthesize parallel systems that achieve desired AFSs.

Some parallel systems, like the soft parallel robots of this paper (Fig. 2), possess wirelike active constraints that are each capable of imparting multiple loads onto the system's stage with loads that are not limited to pure forces along their axes. We will now discuss how to calculate the AFS for these systems. The process is similar for calculating the AFS of parallel systems that possess active constraints that can only impart pure forces along their axes. If an active constraint can impart a pure force on the stage in a different direction than along its axis, then $\mathbf{u}_{(1)}$ from Eq. (11) must be made to point in the direction of this new force load and $q_{(1)}$ must remain zero. If the constraint can impart a load that is a coupled moment and force, then $\mathbf{u}_{(1)}$ from Eq. (11) must be made to point in the direction of this load but $q_{(1)}$ must be set to the

correct moment to force ratio. If the constraint can impart a pure moment load onto the stage, Eq. (11) must be changed to

$$\mathbf{W}_{(1)} = \begin{bmatrix} \mathbf{0} \\ \mathbf{u}_{(1)} \end{bmatrix} \quad (15)$$

where $\mathbf{0}$ is a 3×1 vector of zeroes, $\mathbf{u}_{(1)}$ is again a 3×1 unit vector that points in the direction of the pure moment, and $f_{(1)}$ from Eq. (10) is the scalar magnitude of the pure moment. If a single active constraint can impart multiple loads onto the stage of its system, like the TCA constraints of this paper (Fig. 1), one must identify how many independent loads (i.e., wrench vectors) it can impart on the system's stage and use these vectors to generate multiple twist vectors, $\mathbf{T}_{(ij)}$, to stack inside Eq. (12). The (i) subscript refers to the twist vector's corresponding active constraint labeled (i) and the j subscript refers to the labeled number of one of the multiple independent loads that it can impart on the stage. Previously, for Eq. (12), each twist vector corresponded to a single active constraint because each active constraint could only impart a single load (i.e., a pure axial force) on the system's stage and no j subscript was necessary. Once these changes have been made to the previous equations, Eq. (14) may be applied to determine every twist vector, \mathbf{T}_{AFS} , that lies within the system's AFS as long as $f_{(i)}$ is changed to $f_{(ij)}$ in the equation.

Suppose now we know a particular system's AFS but we wish to determine the load magnitude output vector, $[f_{(1)} \quad f_{(2)} \quad \cdots \quad f_{(C)}]^T$, for actuating a particular twist vector, \mathbf{T} , that lies within the AFS. We could use the following equation:

$$[f_{(1)} \quad f_{(2)} \quad \cdots \quad f_{(C)}]^T = ([\mathbf{T}_{\text{AFS}}]^T [\mathbf{T}_{\text{AFS}}])^{-1} [\mathbf{T}_{\text{AFS}}]^T \mathbf{T} \quad (16)$$

As long as the twist vector, \mathbf{T} , lies within the system's AFS, this equation will yield a correct load magnitude output vector. Suppose for instance, we wished to determine the correct load output vector for actuating the stage of the system in Fig. 5(b) such that it displaces 1 mm in the direction of the black arrow shown. If we construct the appropriate twist vector that models this translational displacement and apply it to Eq. (16), the load magnitude output vector is $[0.19 \text{ N} \quad 0.19 \text{ N} \quad 0.19 \text{ N}]$. The actual force values are not as important to recognize as is their ratio (i.e., 1:1:1). It is this ratio that links the output loads of a system's active constraints to the desired stage motions that lie within the system's AFS.

4 Synthesizing Active Constraint Systems

This section provides systematic steps to help designers synthesize parallel systems that achieve a desired set of actuated motions and consist of wirelike constraints that are only capable of imparting pure forces along their axes to achieve those motions. We will provide two examples to demonstrate the utility of these steps.

Step 1: Identify the desired motions that the system should achieve when its constraints are actuated.

Step 2: Identify the freedom space that results from the linear combination of the twist vectors of these motions. This freedom space will be the system's AFS.

Step 3: Identify the number of independent twist vectors within this freedom space (i.e., m) and consider every freedom space from within the appropriate column of the FACT library [17] that possesses $6 - m$ independent twist vectors (i.e., n from Eq. (1)). Position these freedom spaces such that when their twists are linearly combined with the twists of the AFS, the 6DOF Type 1 freedom space is produced. Select the most promising freedom space that satisfies these conditions and this space will be the system's PFS.

Step 4: Identify the PFS's complementary constraint space.

Step 5: Select m independent constraints from within this constraint space to produce an exactly constrained system. The

axes of the constraints selected must be collinear with the blue constraint lines within the constraint space. If additional constraints are selected, the system will be overconstrained and will be able to be redundantly actuated.

Step 6: Tune the geometric parameters and material properties of the topology synthesized in step 5 using the equations from Sec. 3 such that the system's AFS is positioned desirably with respect to the system's stage.

It is important to recognize that these steps are not always guaranteed to produce a viable design solution. If, however, a solution exists and these steps are correctly applied for each of the finite options provided within the FACT library [17], designers can rapidly identify and compare every possible solution that successfully achieves the desired actuated motions specified in step 1.

4.1 Example 1. We will now demonstrate these steps in the context of an example. Suppose for step 1, we wish to synthesize a system that can be actuated by its constraints to achieve two independent motions—a rotation and a perpendicular translation—as shown on the left side of Fig. 6(a). For step 2, we identify the freedom space that is generated by linearly combining these motions. It consists of an infinite set of parallel rotation lines that lie on a common plane and a translation arrow that is perpendicular to this plane as shown on the right side of Fig. 6(a) and on the left side of Fig. 6(b). This space is the system's AFS and is the 2DOF Type 2 freedom space from the FACT library [17]. For step 3, we recognize that this AFS possesses 2 independent twist vectors (i.e., $m=2$). We also recognize that the 4DOF

Type 2 freedom space, shown in the middle of Fig. 6(b) possesses four independent twist vectors (i.e., $n=4$), which in conjunction with the number of twist vectors within the AFS satisfies Eq. (1) (i.e., $6-4=2$). We also know that when the twist vectors within the 4DOF Type 2 freedom space are linearly combined with the twist vectors within the system's AFS (as long as the spaces are positioned as they are in Fig. 6(b)), the resulting freedom space is the 6DOF Type 1 freedom space shown on the right side of Fig. 6(b). Thus, the 4DOF Type 2 freedom space satisfies the conditions in step 3 and is a potential candidate as the final system's PFS. For step 4, we use the FACT library [17] to identify this space's complementary constraint space shown in Fig. 6(c). For step 5, we recognize that this constraint space possesses two independent constraints within its geometry. We thus synthesize a parallel system that possesses two active wire constraints with axes that are aligned with two of the blue constraint lines from within the selected constraint space (Fig. 6(d)). For step 6, we arbitrarily select a material with a Young's Modulus, E , of 68 GPa and a shear modulus, G , of 25 GPa, and then tune the system's other geometric parameters such that the desired AFS lies half way down the length of the wire flexures (Fig. 6(e)). Note that all the motions within the system's AFS, including the two desired motions in Fig. 6(a), can successfully be achieved by actuating the system's two wire constraints with various force's along their axes. Note also that the final system will possess four passive DOFs—two orthogonal rotations and two orthogonal translations. These DOFs are the independent twist vectors within the system's PFS (Fig. 6(c)).

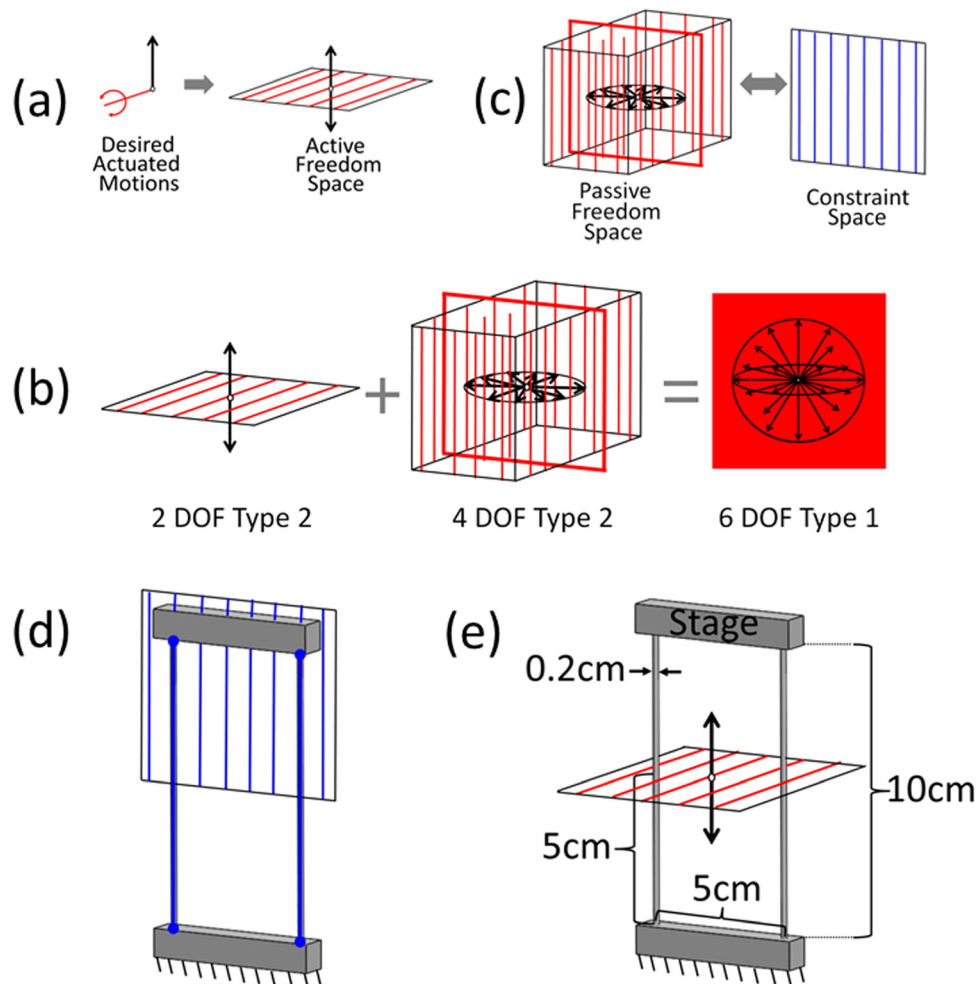


Fig. 6 AFS (a), PFS that satisfies conditions (b), its constraint space (c), topology selected from that space (d), and tuned parameters (e)

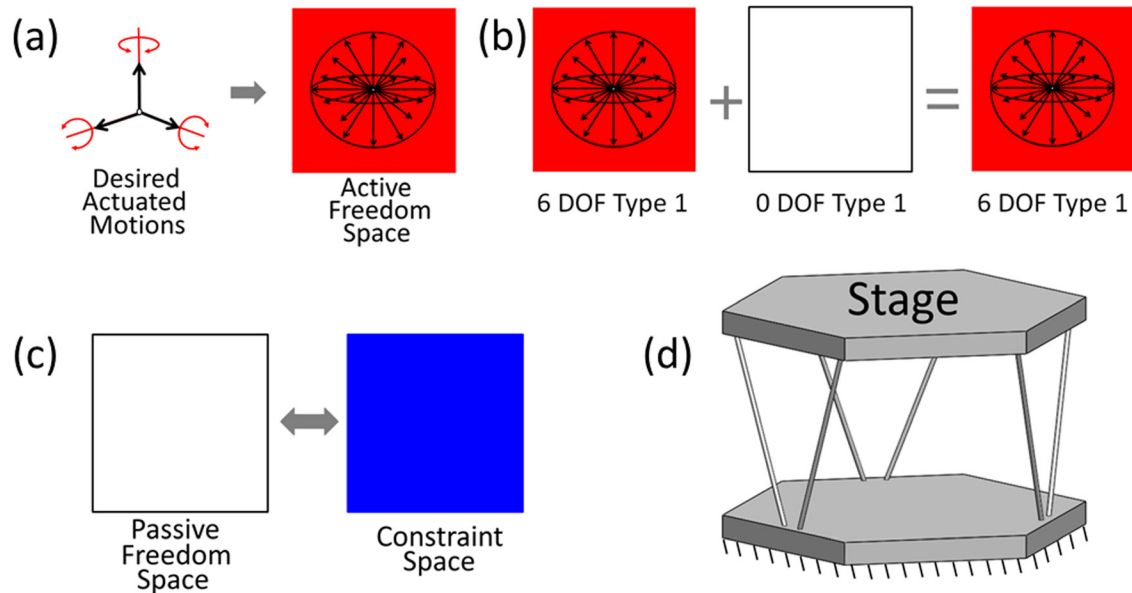


Fig. 7 AFS (a), PFS that satisfies conditions (b), its constraint space (c), and topology selected (d)

4.2 Example 2. We now do a second example to demonstrate the practical utility of this theory. Suppose we wish to synthesize a system that can be actuated by its constraints to achieve six independent motions—three rotations and three translations—as shown on the left side of Fig. 7(a). The AFS that results from the linear combination of these six twist vectors is the 6DOF Type 1 freedom space in the FACT library shown on the right side of Fig. 7(a) and on the left side of Fig. 7(b). We thus recognize that this AFS possesses 6 independent twist vectors (i.e., $m=6$). The only freedom space that possesses zero independent twist vectors (i.e., $n=0$) to satisfy Eq. (1) in conjunction with the number of independent twist vectors within the system's AFS (i.e., $6-0=6$) is the 0DOF Type 1 freedom space from the FACT library shown in the middle of Fig. 7(b) and on the left side of Fig. 7(c). This freedom space is an empty white box that possesses no DOFs and is the only PFS option possible. We confirm that this PFS combined with the 6DOF Type 1 AFS produces the 6DOF Type 1 freedom space as shown in Fig. 7(b). We then use the FACT library from Ref. [17] to identify this PFS's complementary constraint space, which consists of every blue constraint line in three-space. This constraint space is represented by the filled-in blue box on the right side of Fig. 7(c). We recognize that this constraint space consists of six independent wrench vectors. We select six active wire constraints with axes that correspond with the constraint lines of six independent pure force wrench vectors within the constraint space of the system as shown in Fig. 7(d). Note that the resulting system is a Stewart Platform [20]. It is totally exactly constrained and thus possesses no passive DOFs. If we set the material properties and geometric parameters of its active constraints, we can apply Eq. (16) to determine their output load magnitude ratios that successfully achieve any twist vector within the system's AFS. Since this AFS includes all possible twists in three-space, designers can actuate the system's stage to move with any desired motion.

5 Modeling TCA

In this section, we experimentally justify modeling TCAs as effective wire flexures that possess high axial stiffness compared with all other directions. We thus conclude that the principles discussed in Secs. 2–4, which are intended for analyzing and synthesizing parallel systems that consist of active wire flexures that impart pure forces along their axes only, may also be applied to analyzing and synthesizing soft parallel robots that consist of

TCAs where all three chambers are pressurized the same amount. We also experimentally determine a TCA's effective material properties such that the mathematics provided in Sec. 2 can be used to model their behavior.

5.1 TCA Fabrication. Each TCA was molded using Mold-Star 16 FAST silicone rubber from Smooth-On and their geometric parameters are shown in Fig. 8(a). The TCAs were fabricated in a high density polyethylene mold. The cavities in each actuator were created using steel rods secured on both ends. The mold was filled from a single point using two peristaltic pumps, eight inches of static inline mixers, and sufficient reservoirs of both part A and part B of the silicone rubber to fill the mold. By maintaining both pumps at the same volumetric flow rate it was possible to ensure consistent material properties and effective mixing. We found this method to be superior to hand mixing the two parts because it ensured similar material properties between batches and allowed for the production of the required amount of silicone which could be visually regulated by the operator. Utilizing this setup with static inline mixers precluded the formation of air bubbles, which had an issue in earlier hand mixed samples. Air bubbles compromise homogeneity of the structure and ultimately resulted in

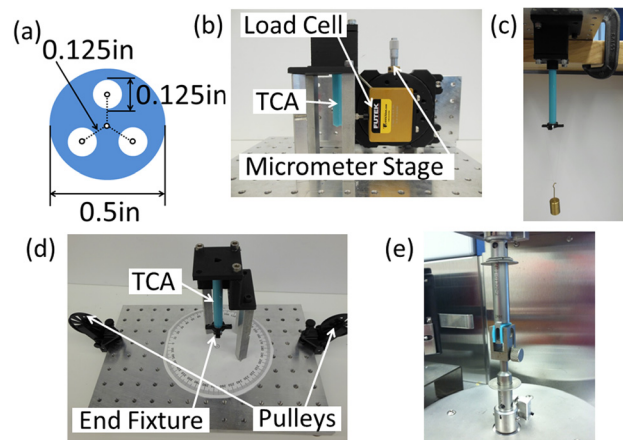


Fig. 8 Cross section of a TCA (a), transverse linear stiffness test (b), axial stiffness test (c), torsional stiffness test (d), and calculating the TCA's material properties (e)

unexpected behavior that invariably led to rupture. Mixing by machine also improved material consistency, which improved the reliability of the actuators and uniformity across fabrication batches.

Once the TCAs were fabricated, they were sealed and plumbed. The TCAs were sealed at one end by covering the end with a layer of silicon adhesive (Sil-Poxy from Smooth-On). This adhesive created an airtight seal over one end of the TCA and facilitated the creation of three internal pressure chambers. Each chamber was plumbed with platinum cured silicone tubing with an outside diameter of 1/8 in. by adhering the tubing to the open end of each chamber with silicone adhesive. This tubing was stiffer than the silicone into which it was inserted and the addition of this material thickness into the channel further increased the stiffness of the attachment area. This increase in stiffness prevented the air from inflating the plumbing tubing when the system was pressurized. Each chamber was pressurized until the TCA bent to extreme angles to detect leaks. Detected leaks were then resealed and tested again.

A male-barbed-to-male luer connector was inserted into the plumbing tubing for each actuation channel. The luer fitting allowed connection to simple polyvinyl chloride tubing with luer fittings for the distribution of air pressure. For testing of more than a single channel of pressure, a manifold was constructed to maintain the same pressure along a number of connections.

5.2 Static Testing. The TCAs were placed in several testing configurations to measure static force displacement characteristics in various directions. In Sec. 5.2.1–5.2.3, we describe the testing procedures. Stiffness values from the testing are summarized in Table 1.

5.2.1 Transverse Linear Stiffness. A transverse force was applied perpendicular to the longitudinal axis of the TCA using a micrometer stage (ThorLabs Model XYR1). The resistive force was captured with a load cell (FUTEK LRF400) mounted between the TCA and the micrometer stage (Fig. 8(b)). The micrometer stage was advanced in increments of 0.025 in. and the resulting resistive force was measure by the load cell. A linear trend in force verses displacement resulted when testing the TCA from rest to 0.5 in. of displacement. This process was repeated for the TCA rotated 90 deg from its original position to measure the stiffness in the other transverse direction. As indicated in Table 1, the transverse stiffness in both directions are nearly identical similar to a regular cylindrical wire flexure.

5.2.2 Axial Stiffness. To determine the linear axial stiffness we hung weights from the TCA through a fixture placed on the end of the TCA (Fig. 8(c)). The load cell was not used for this case because the forces needed to appreciably stretch the TCA along its axis given its cylindrical geometry were substantially larger than those used to determine the transverse stiffness. The extension of the actuator was recorded for different loads. The resulting force verses displacement plot was linear, and showed an increase in stiffness that was two orders of magnitude greater than the transverse stiffness (see Table 1).

5.2.3 Bending Angular Stiffness and Torsional Stiffness. The test necessary to measure angular stiffness in bending and torsion

required a more complex setup to ensure that only pure moments were applied to the TCA. The same end fixture from the axial stiffness test was used (Fig. 8(c)). Fishing lines were tied to the end fixture at two locations equidistant from the central axis of the TCA. Equal weights were hung from the ends of each fishing line but one of the lines was redirected through frictionless pulleys to reverse the direction of its force on the TCA. In this way, pure bending moments were imparted on the TCA. The test setup for measuring torsional stiffness is shown in Fig. 8(d). Again two fishing lines were used with pulleys to impart a torsional moment at the end of the TCA. The resulting axial rotations were measured using a protractor. Because the TCAs are made of silicone rubber with a low modulus of elasticity, the weights of the masses hung from the fishing lines were verified using a high precision electronic balance. The results of both tests demonstrate linear relationships between moment and angular rotation in all directions. As expected, the angular stiffness that corresponds with the two orthogonal bending directions is nearly identical and the torsional stiffness is the same order of magnitude (see Table 1).

5.3 Modeling TCAs as Wire Flexures. The stiffness values provided in Table 1 demonstrate that the constraint behavior of TCAs are similar to those of wire flexures (i.e., they are multiple orders of magnitude stiffer along their axis than in any other direction). Thus, similar to wire flexures, a TCA can be modeled using a single blue constraint line that is coincident with the TCA's central axis. Thus, as long as all three chambers within a TCA are restricted to be pressurized the same amount such that it can only impart a pure force along its axis, all aspects of the theory previously provided in Secs. 2–4 can be applied to parallel systems that consist of TCA's instead of active wire flexures. It is important to note, however, that if the TCAs' three chambers are allowed to be pressurized different amounts such that nonaxial forces or other moments can be imparted on the system's stage, the theory provided at the conclusion of Sec. 3 can be applied to calculate the system's new AFS and analyze the system's resulting kinematics.

Although we have validated the fact that the constraint behavior of a TCA is similar to that of a wire flexure, constructing the stiffness matrix of Eq. (5) to correctly model the TCA as a cylindrical wire requires that the TCA's effective geometric parameter's (i.e., its length, l , and diameter, d) and material properties (i.e., Young's modulus, E , and shear modulus, G) are identified. Although each TCA possesses three hollow cylindrical chambers, we model the entire TCA as if it is a solid cylinder by using its actual length and diameter in Eq. (5). As we will later show, this assumption causes minimal error in our mobility analysis. To determine the TCA's effective material properties, we used a Rheometrics System Analyzer (RSA3) from TA Instruments. The TCA's Young's modulus was measured using a tensile test arrangement in which a rectangular piece of material with a known cross sectional area and length was gripped and stretched. The forces and displacements were then recorded and used to calculate the modulus. The calculated modulus is $E = 316$ kPa. Finding the TCA's shear modulus required the use of a "shear sandwich" fixture as shown in Fig. 8(e). With this setup, two identical pieces of material were compressed around a central shaft with a flattened head. This shaft was displaced vertically at various frequencies to determine a dynamic shear modulus for the material. Because shear modulus was found to be dependent on the rate of strain, the Young's modulus was also measured using dynamic testing so that the results could be compared and used to calculate a Poisson's ratio for the material. The test frequencies were varied from 0.1 Hz to 100 Hz. Over this range, the Young's modulus was determined not to vary significantly with changes in frequency. The shear modulus value at 1 Hz was selected as the TCA's effective shear modulus because the rates that TCAs are inflated to actuate a robot's stage are generally slow. This effective shear modulus is $G = 117.55$ kPa.

Table 1 Stiffness calculated from TCA testing

Loading case	Stiffness
Transverse linear stiffness 1	4.4405 N/m
Transverse linear stiffness 2	4.2648 N/m
Torsional stiffness	0.0018 N m/rad
Bending angular stiffness 1	0.0049 N m/rad
Bending angular stiffness 2	0.0047 N m/rad
Axial stiffness	228.35 N/m

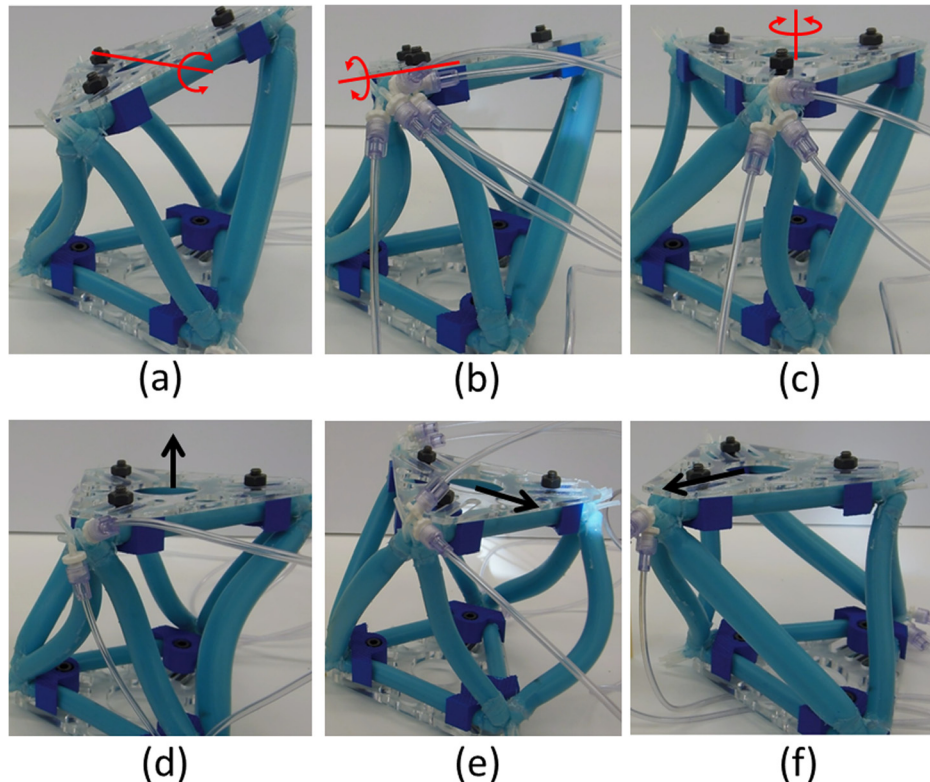


Fig. 9 6DOFs achieved by hexapod robot—three rotations (a)–(c), and three translations (d)–(f)

6 Verifying FACT's Kinematic Predictions Using Two Soft Robot Examples

In this section, two fabricated FACT-synthesized soft parallel robots that consist of TCAs are actuated to demonstrate their intended kinematics. One of the examples is similar to the wire-flexure-based system in Fig. 7(d) and the other is similar to the wire-flexure-based system in Figs. 3–5. The analytical tools of this paper are then used to predict the resulting stage kinematics when one of the TCAs within the system of the second example is inflated. FEA and experimental data are used to verify and validate the accuracy of these analytical tools.

Both robot examples were constructed by joining several TCAs to a rigid base. They were then secured to a test platform and air pressure was applied within individual TCA chambers to produce the system's motions. A constant air pressure was applied throughout the system so that all actuators received the same pressure to simplify the experimental setup. This approach was sufficient to demonstrate the mobility in each example.

It is important to note that although we limited the TCAs within the examples of this section to only impart pure forces along their axes (i.e., all three of their chambers were pressurized the same amount), in practice the chambers within TCAs could be pressurized differently to impart other forces or moments onto their stage. We limit the TCAs in this section to axial forces only because we wish to verify the kinematics predicted by the analytical tools of Secs. 2–4, which largely assume active constraints that can only impart pure forces along their axes. Although the conclusion of Sec. 3 does provide the theory necessary to analyze soft parallel robots made of TCAs with chambers that are subject to different pressures, synthesizing and more rigorously analyzing such robots is the focus of a sequel paper.

The first example utilizes the same topology as the hexapod designed in Sec. 4.2 (Fig. 7(d)) but this example possesses six TCAs in place of the six active wire constraints (see Fig. 2). The clamps shown in Fig. 2 were made by 3D printing small fixtures

that were then connected to a thin piece of laser cut acrylic. This robot possesses six active DOFs and zero passive DOFs as noted in the example of Sec. 4.2. The six active DOFs were demonstrated by inflating the TCA's as shown in Fig. 9.

The second example utilizes the same topology as the three-legged system shown in Figs. 3–5, but this example possesses three TCAs in place of the three active wire constraints as shown in Fig. 10. Consequently, the example of Fig. 10 possesses the same PFS (Fig. 3(b)) and the same AFS (Fig. 5(b)) as long as each TCA is only allowed to impart axial forces on the system's stage by inflating all three of its chambers with the same amount of pressure. The geometric parameters of this example are labeled in Fig. 10. The orientations of the three chambers within each of the system's three TCAs are also shown on the right side of this figure. Using these parameters and the TCA's material properties provided in Sec. 5.3, one can apply Eq. (10) to calculate the theoretical twist vector, $\mathbf{T}_{(1), \text{Analytical}}$, that results by inflating all three chambers within the TCA labeled (1) in Fig. 11(a) the same

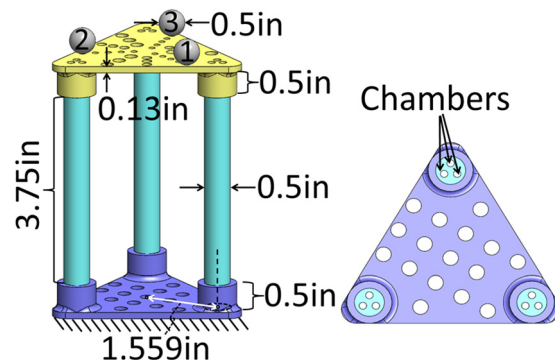


Fig. 10 Geometric parameters for the three-legged soft robot

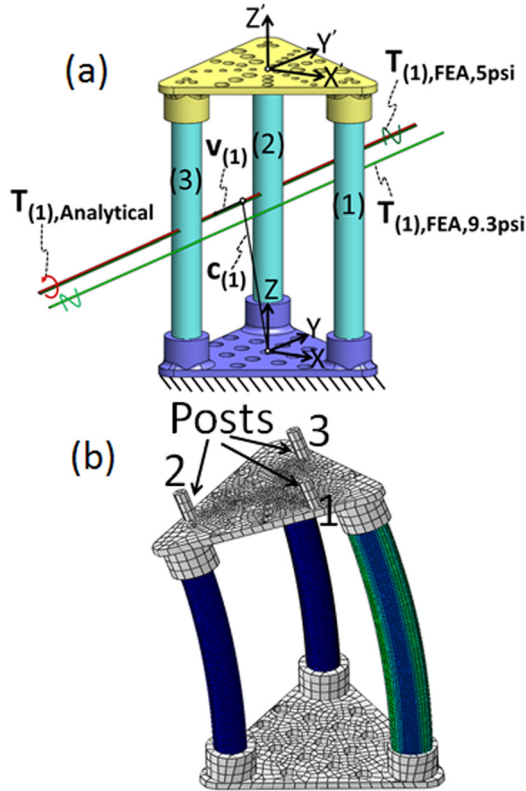


Fig. 11 Twist vectors that describe the analytical and FEA results drawn to scale (a), and FEA verification (b)

amount. The resulting twist vector is a rotational line, shown red in Fig. 11(a), about which the system's stage rotates in response to the axial force imparted on the system's stage by TCA (1). The specific location and orientation of this line's rotational axis can be determined by decomposing this resulting twist vector according to the definition of a general twist, \mathbf{T} , given by

$$\mathbf{T} = \Delta\theta \begin{bmatrix} \mathbf{v} \\ \mathbf{c} \times \mathbf{v} + p\mathbf{v} \end{bmatrix} \quad (17)$$

where \mathbf{c} is any 3×1 location vector that points from the system's coordinate system (labeled X, Y, and Z in Fig. 11(a)) to any point along the twist's axis. The vector \mathbf{v} is a 3×1 unit vector that points along the twist's axis in the direction about which the stage rotates. The scalar value $\Delta\theta$ is the magnitude of the stage rotation in radians about the twist's axis, and p is the twist's pitch value, which is the ratio of the distance the system's stage translates along the twist's axis over the radians the stage simultaneously rotates about the same axis. In the case of the twist caused by inflating all three chambers using the same pressure within TCA (1), the resulting twist vector, $\mathbf{T}_{(1),Analytical}$, is a pure rotation and thus possesses a pitch, $p_{(1)}$, of zero. This twist's axial unit vector, $\mathbf{v}_{(1)} = [v_{x(1)} \ v_{y(1)} \ v_{z(1)}]$, its rotational magnitude, $\Delta\theta$, and one possible location vector, $\mathbf{c}_{(1)} = [c_{x(1)} \ c_{y(1)} \ c_{z(1)}]$, are all provided in Table 2. According to this paper's analytical tools, the location and orientation of the twist's rotational axis (i.e., $\mathbf{c}_{(1)}$, $\mathbf{v}_{(1)}$, and $p_{(1)}$) are not affected by the magnitude of the TCA's axial force (i.e., $f_{(1)}$ from Eq. (10)). Only the twist's rotational magnitude, $\Delta\theta$, is affected by this force. Two different axial forces with magnitudes of 0.0010 lbf and 0.0118 lbf were used in Eq. (10) to calculate the stage's corresponding rotational magnitudes, 0.0299 rad and 0.3693 rad, respectively, as shown in the columns titled "Analytical stage motion" in Table 2. The reason for using these two specific forces will be discussed shortly. We define another coordinate system that is positioned on the top surface of the

Table 2 A comparison of the stage's analytical and FEA motion results caused by pressurizing all three chambers in leg (1)

Parameters	Analytical stage motion		FEA stage motion	
	0.0010 lbf	0.0118 lbf	5 psi	9.3 psi
Leg (1) axial load				
$c_{x(1)}$ (in.)	−0.7862	−0.7862	−0.7608	−0.4142
$c_{y(1)}$ (in.)	0	0	0	0
$c_{z(1)}$ (in.)	2.3750	2.3750	2.3551	2.2220
$v_{x(1)}$	0	0	0.0004	−0.0034
$v_{y(1)}$	−1	−1	−1.0000	−1.0000
$v_{z(1)}$	0	0	0.0003	−0.0001
$p_{(1)}$ (in./rad)	0	0	−0.0005	−0.0032
$\Delta\theta_{(1)}$ (rad)	0.0299	0.3693	0.0299	0.3693
X' rotation (rad)	0	0	0.0000	−0.0013
Y' rotation (rad)	−0.0299	−0.3693	−0.0299	−0.3693
Z' rotation (rad)	0	0	0.0000	−0.0000
X' translation (in.)	−0.0749	−0.9252	−0.07553	−0.9817
Y' translation (in.)	0	0	−0.0000	0.0045
Z' translation (in.)	0.0235	0.2904	0.0228	0.1530

system's stage with axes labeled X', Y', and Z' in Fig. 11(a) to more clearly define the effect $\mathbf{T}_{(1),Analytical}$ has on the system's stage directly. The amount the stage rotates and translates about and along the axes of this new coordinate system as a result of this twist vector is provided in the lower portion of the same columns in Table 2.

FEA was used (i.e., ABAQUS) to verify these resulting stage motions for similar loading conditions. The TCA actuators were modeled as a hyperelastic material using the two-parameter Mooney–Rivlin model. The two material parameters were determined by experimentally fitting the uniaxial loading data on a single unpressurized TCA member. They were found to be $C1 = 0.0429$ MPa, and $C2 = -0.0009$ MPa. The rigid segments that constitute the top and bottom stage were modeled as a considerably stiffer linear elastic material ($E = 200$ GPa, $\nu = 0.3$). The rigid segments were assembled on the TCA using a tie-constraint, which bonds the nodes at the ends of the TCA to the rigid stage. Special attention is paid to the mesh sizes of the TCA to ensure that all elements have close to a unit aspect ratio. The mesh is shown in Fig. 11(b). The nodes of the bottom stage were constrained to be fixed in all directions. Uniform pressures of 5 psi and then 10 psi were applied on all the three pockets of the TCA including the parts of the rigid stage that are exposed to the TCA. ABAQUS subdivided the load into a number of substeps and used a nonlinear solver to solve for the deformed configuration of the stage for each step. While ABAQUS adjusted the step sizes automatically to ensure convergence, the minimum increment size was limited to 10^{-10} , and the maximum was limited to 0.1. Furthermore, the maximum number of increments was limited to 10^4 . It was found that application of the 10 psi load did not result in convergence irrespective of decreasing step sizes. The closest pressure value for which the system converged was at 9.3 psi.

The locations of the top most points of the three posts (Fig. 11(b)) were determined when all the walls within the three chambers of TCA (1) were loaded with 0 psi, 5 psi, and 9.3 psi of pressure. These locations are provided in Table 3. Note that the posts are labeled 1–3 in Fig. 11(b). Since the system's stage is effectively rigid, these three locations fully define the location and orientation of the stage at any of its three actuated positions. A MATLAB script was written that assigns a coordinate system with three orthogonal unit vectors to the stage given three unique locations anywhere on the stage. Using standard kinematic theory [21], this script is able to generate a single displacement–twist vector that approximates how the stage of any general system moved from one position to another. This script requires two sets of three stage points corresponding to two stage positions to generate any one displacement–twist vector. It is important that the

Table 3 Locations of the top most points of the posts (Fig. 11(b)) determined computationally using FEA for different pressures within leg (1)

Leg (1) pressures (psi)	Post 1			Post 2			Post 3		
	X (in.)	Y (in.)	Z (in.)	X (in.)	Y (in.)	Z (in.)	X (in.)	Y (in.)	Z (in.)
0	1.1549	−0.4784	5.1300	−0.9917	−0.7610	5.1300	−0.1632	1.2393	5.1300
5	1.0719	−0.4784	5.1873	−1.0736	−0.7610	5.1231	−0.2455	1.2393	5.1479
9.3	0.0809	−0.4736	5.7101	−1.9209	−0.7566	4.9356	−1.1478	1.2438	5.2322

same three points on the stage are used for both stage positions. The script would, for instance, require the locations of the points on top of the three posts at 0 psi before the stage moved, and then at 5 psi after it moved to generate $\mathbf{T}_{(1),\text{FEA},5\text{ psi}}$. Or the script would require the locations of the points on top of the three posts at 0 psi and then at 9.3 psi to generate $\mathbf{T}_{(1),\text{FEA},9.3\text{ psi}}$. The twist vectors generated by this script are exact when the stage moves an infinitesimally small amount from the initial position to its actuated position. Unfortunately, however, the script becomes less accurate the larger the actuated position is from the initial position. The reason is that a body that traverses a finite path through space can usually only be fully described using a sequence of infinitesimally small displacement–twist vectors that change with every advancing infinitesimal increment of time. The true nature of large motion paths are thus not accurately captured using the single averaged displacement–twist vector generated by this script. Since the tools of this paper are intended for predicting small displacements, however, the written MATLAB script is sufficient for our purposes.

This script was used to calculate the twist vectors, $\mathbf{T}_{(1),\text{FEA},5\text{ psi}}$ and $\mathbf{T}_{(1),\text{FEA},9.3\text{ psi}}$, from the data collected in Table 3. These vectors were then decomposed using Eq. (17) and their parameters are given in the two columns labeled “FEA stage motion” corresponding to the two different pressures in Table 2. The resulting stage translations and rotations along and about the axes labeled X' , Y' , and Z' in Fig. 11(a) caused by these two twist vectors are also provided in the lower portion of the same columns. Using the analytical tools of this paper, it was determined that an axial TCA force, $f_{(1)}$, of 0.0010 lbf produced the same rotational magnitude, $\Delta\theta$, as did a pressure of 5 psi within all three chambers of TCA (1) using FEA. Similarly, it was also determined that an axial TCA force of 0.0118 lbf produced the same rotational magnitude as did a pressure of 9.3 psi within all three chambers of the same TCA using FEA. Thus, by comparing the results of the column titled “0.0010 lbf” in Table 2 with the results of the column titled “5 psi,” and by comparing the results of the column titled “0.0118 lbf” with the results of the column titled “9.3 psi,” one can compare how well FEA verified the predicted kinematics calculated by the analytical tools of this paper. The FEA results can also be visually compared to the analytical results by incorporating the axes of the two twist vectors into the system’s computer-aided design (CAD) model by representing them as long thin cylinders colored different shades of green as shown in Fig. 11(a).

The results of Fig. 11(a) and Table 2 demonstrate how well FEA verifies the accuracy of the analytical tools of this paper. It is important to reemphasize that according to the foundational assumptions of the theory provided in Sec. 3, the analytical tools of this paper are expected to be accurate for small stage displacements only. Furthermore, we would expect that the MATLAB script that calculates a single twist vector that represents the motion from one stage position to another is also only accurate for small stage displacements as described previously. Thus, we would expect the analytical results of Fig. 11(a) and Table 2 to be verified by the FEA results with less discrepancies for smaller TCA pressures. Note from Fig. 11(a), that the axis of $\mathbf{T}_{(1),\text{FEA},5\text{ psi}}$ is almost collinear with the axis of $\mathbf{T}_{(1),\text{Analytical}}$ at 5 psi of TCA pressure. Note also from Table 2 that according to FEA, the

analytical prediction for the amount the stage translates along the X' axis at 5 psi of TCA pressure is within 0.8% error and the amount the stage translates along the Z' axis at the same pressure is within 3.1% error. Thus, these results strongly verify the accuracy of this paper’s tools. Note from Fig. 11(a), however, that the axis of $\mathbf{T}_{(1),\text{FEA},9.3\text{ psi}}$ is much farther from the axis of $\mathbf{T}_{(1),\text{Analytical}}$ at 9.3 psi of TCA pressure. Furthermore, note from Table 2 that according to FEA, the analytical prediction for the amount the stage translates along the X' axis at 9.3 psi of TCA pressure is within 5.8% error but the amount the stage translates along the Z' axis at the same pressure is 89.9% error. Such a large stage displacement error at 9.3 psi of TCA pressure is consistent with what we would expect for such a large stage rotation (~ 0.37 rad or ~ 21 deg) since our analytical tools are not correct for large displacements. These findings provide a sense for how large the stage displacements can be before they are obviously too large to be accurately predicted using this paper’s tools.

Experimental data was also collected using the fabricated soft robot shown in Fig. 12(a) to validate the predicted kinematics of this paper’s analytical tools for similar loading conditions. The dimensions of this robot are the same as those given in Fig. 10. The robot’s stage and fixed ground were 3D printed using

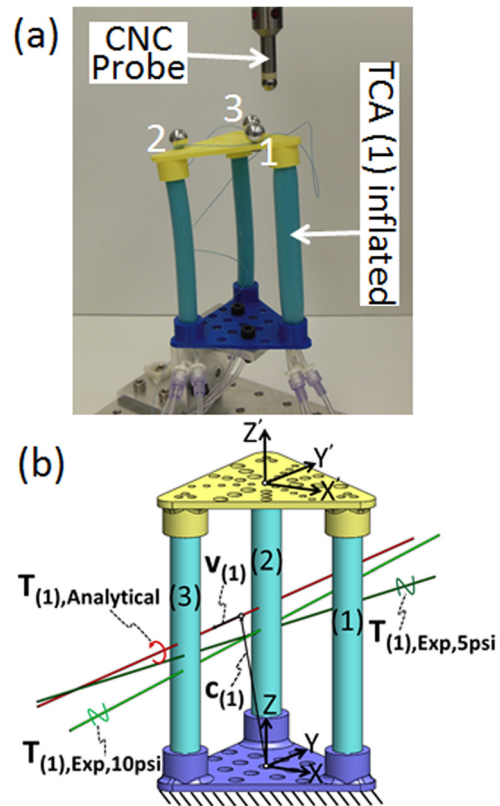


Fig. 12 Experimental setup (a), and twist vectors that describe the analytical and experimental results drawn to scale (b)

Table 4 Locations of the central points of the spheres (Figs. 10 and 12(a)) measured using a CNC probe for different pressures within leg (1)

Leg (1) pressures (psi)	Sphere 1			Sphere 2			Sphere 3		
	X (in.)	Y (in.)	Z (in.)	X (in.)	Y (in.)	Z (in.)	X (in.)	Y (in.)	Z (in.)
0	1.1865	−0.4290	5.0830	−0.9480	−0.8250	5.0740	−0.2190	1.2130	5.0540
5	1.1655	−0.4255	5.0960	−0.9745	−0.8240	5.0720	−0.2425	1.2150	5.0580
10	1.0470	−0.4280	5.1680	−1.0950	−0.8230	5.0630	−0.3565	1.2140	5.0780

polylactic acid. To measure the resulting stage motions caused by inflating all the chambers within the TCA labeled (1) in Fig. 12(b), three spheres were affixed to the robot's stage as shown in Figs. 10 and 12(a). Similar to the three posts used in the FEA verification, the locations of the central points of these three spheres were measured using an electronic probe attached to a computer numerical control (CNC) three axis milling machine, which illuminated when it contacted the spheres. Similar to how a coordinate measuring machine functions, the locations of these points could be determined by touching the spheres multiple times along each axis. The measured locations of the central points of the spheres are provided in Table 4 when the three chambers within TCA (1) were all inflated with 0 psi, 5 psi, and 10 psi of pressure. Note that the spheres are labeled 1–3 in Figs. 10 and 12(a). The same MATLAB script described previously was then used to calculate the stage's two twist vectors, $\mathbf{T}_{(1),\text{Exp},5\text{ psi}}$ and $\mathbf{T}_{(1),\text{Exp},10\text{ psi}}$, which represent the axis about which the stage rotates from the rest position (i.e., 0 psi) to the 5 psi position and from the rest position to the 10 psi position, respectively. These twists were decomposed using Eq. (17) and their parameters are given in the two columns labeled "Experimental stage motion" corresponding to these two different pressures in Table 5. The resulting stage translations and rotations along and about the axes labeled X' , Y' , and Z' in Fig. 12(b) caused by these two twist vectors are also provided in the lower portion of the same columns. Using the analytical tools of this paper, it was determined that an axial TCA force, $f_{(1)}$, of 0.0002 lbf produced the same rotational magnitude, $\Delta\theta$, as did a pressure of 5 psi within all three chambers of TCA (1) using the experimental setup of Fig. 12(a). Similarly, it was also determined that an axial TCA force of 0.0014 lbf produced the same rotational magnitude as did a pressure of 10 psi within all three chambers of the same TCA. Thus, by comparing the results of the column titled "0.0002 lbf" in Table 5 with the

results of the column titled "5 psi," and by comparing the results of the column titled "0.0014 lbf" with the results of the column titled "10 psi," one can compare how well experimental data validated the predicted kinematics calculated by the analytical tools of this paper. The experimental results can also be visually compared to the analytical results by incorporating the axes of the two twist vectors, $\mathbf{T}_{(1),\text{Exp},5\text{ psi}}$ and $\mathbf{T}_{(1),\text{Exp},10\text{ psi}}$, into the system's CAD model by representing them as long thin cylinders colored different shades of green as shown in Fig. 12(b).

The results of Fig. 12(b) and Table 5 demonstrate how well the experimental results validate the accuracy of the analytical tools of this paper. Note that the axes of $\mathbf{T}_{(1),\text{Exp},5\text{ psi}}$ and $\mathbf{T}_{(1),\text{Exp},10\text{ psi}}$ are not as parallel with the axis of $\mathbf{T}_{(1),\text{Analytical}}$ as the FEA results shown Fig. 11(a). This observation is likely due to the asymmetries inherent within the fabricated system. No two TCAs are exactly alike and it is difficult to assemble them such that they are perfectly parallel. Furthermore, the spheres attached to the stage are asymmetrically arranged such that their weight may have loaded the stage in a way that was not accounted for by the analytical approach of this paper. The locations measured for the central points of the spheres also possess some degree of error due to the CNC machine's resolution limitations and the fact that touching the spheres may have caused their location to shift slightly. In spite of these potential shortcomings, however, the analytical prediction for the amount the stage translates along the X' axis at 5 psi of TCA pressure according to Table 5 is within 12% error and the amount the stage translates along the Z' axis at the same pressure is within 10% error. Note also from Table 5 that the analytical prediction for the amount the stage translates along the X' axis at 10 psi of TCA pressure is within 14% error and the amount the stage translates along the Z' axis at the same pressure is within 8% error. Note that the experimental results acceptably validate the analytical results for both 5 psi and 10 psi of TCA pressure, whereas the FEA results showed a large discrepancy at 9.3 psi of pressure. The reason is that 9.3 psi of TCA pressure in the FEA simulation produced much more stage rotation (~ 0.37 rad) than did 10 psi of TCA pressure within the experimental setup (~ 0.04 rad). Thus, the experimental results produced small enough stage displacements to validate the analytical predictions, which are correct for small displacements only. The primary reason for the large rotational magnitude discrepancy between the FEA and experimental results for similar loading pressures is that the FEA simulation assumed that the TCA chambers span the entire length of the TCA. In reality, however, the effective length of these chambers is shortened by the stiff tube inserted into one end and by the sealant that plugs them at the other end. This shorter chamber length would cause the TCA to axially expand less for the same pressure and the FEA simulation does not take this into account. It is also important to note that we did not directly measure the pressures inside each chamber of our test setup, so it is difficult to know whether the actual pressures inside each chamber were what we intended or if they were compromised by leaks. Fortunately, for the purposes of this paper, however, validating the axis about which the stage is predicted to rotate by this paper's tools through experimentation or FEA is possible regardless of the stage's specific displacement

Table 5 A comparison of the stage's analytical and experimental motion results caused by pressurizing all three chambers in leg (1)

Parameters	Analytical stage motion		Experimental stage motion	
	0.0002 lbf	0.0014 lbf	5 psi	10 psi
Leg (1) axial load				
$c_{x(1)}$ (in.)	−0.7862	−0.7862	−0.7710	−0.7258
$c_{y(1)}$ (in.)	0	0	0	0
$c_{z(1)}$ (in.)	2.3750	2.3750	2.0380	1.9694
$v_{x(1)}$	0	0	0.0644	0.0230
$v_{y(1)}$	−1	−1	−0.9934	−0.9993
$v_{z(1)}$	0	0	0.0951	−0.0284
$p_{(1)}$ (in./rad)	0	0	−0.5161	−0.1482
$\Delta\theta_{(1)}$ (rad)	0.0070	0.0446	0.0070	0.0446
X' rotation (rad)	0	0	0.0004	0.0010
Y' rotation (rad)	−0.0070	−0.0446	−0.0069	−0.0446
Z' rotation (rad)	0	0	0.0007	−0.0013
X' translation (in.)	−0.0175	−0.1117	−0.0199	−0.1299
Y' translation (in.)	0	0	0.0028	0.0027
Z' translation (in.)	0.0055	0.0351	0.0050	0.0325

magnitudes as long as they are small compared to the size of the system.

7 Conclusions

The principles of FACT have been adapted and applied to the analysis and synthesis of actively constrained parallel systems that consist of wirelike constraints that both passively guide the system's DOFs, and actively impart forces along their axes to actuate the system's stage with other desired motions. The concepts of passive and AFSs are introduced as tools to aid in this analysis and synthesis process. These principles have been adapted to enable the design and analysis of parallel soft robots that consist of TCA active constraints (i.e., cylindrical soft constraints that possess three axisymmetric chambers, which can be pressurized independently to cause the constraint to impart complex loads onto a robot's stage). Example systems have been designed, built, and tested to validate the theory.

References

- [1] Trivedi, D., Rahn, C. D., Kierb, W. M., and Walker, I. D., 2008, "Soft Robotics: Biological Inspiration, State of the Art, and Future Research," *Appl. Bionics Biomech.*, **5**(3), pp. 99–117.
- [2] Iida, F., and Laschi, C., 2011, "Soft Robotics: Challenges and Perspectives," *Procedia Comput. Sci.*, **7**, pp. 99–102.
- [3] Kim, S., Laschi, C., and Trimmer, B., 2013, "Soft Robotics: A Bioinspired Evolution in Robotics," *Trends Biotechnol.*, **31**(5), pp. 287–294.
- [4] Morin, S. A., Shepart, R. F., Kwok, S. W., Kwok, S. W., Stokes, A. A., Nemiroski, A., and Whitesides, G. M., 2012, "Camouflage and Display for Soft Machines," *Science*, **337**(6096), pp. 828–832.
- [5] McMahn, W., Chitrakaran, V., Csencsits, M., Dawson, D., Walker, I. D., Jones, B. A., Pritts, M., Dienno, D., Grissom, M., and Rahn, C. D., 2006, "Field Trials and Testing of the OctArm Continuum Manipulator," 2006 IEEE International Conference on Robotics and Automation (ICRA 2006), Orlando, FL, May 15–19, pp. 2336–2341.
- [6] Bishop-Moser, J., Krishnan, G., Kim, C., and Kota, S., 2012, "Design of Soft Robotic Actuators Using Fluid Filled Fiber-Reinforced Elastomeric Enclosures in Parallel Combinations," 2012 IEEE/RSJ International Conference on Intelligent Robots and Systems (IROS 2012), Vilamoura, Portugal, Oct. 7–12, pp. 4264–4269.
- [7] Hirai, S., Cusin, P., Tanigawa, H., Masui, T., Konishi, S., and Kawamura, S., 2000, "Qualitative Synthesis of Deformable Cylindrical Actuators Through Constraint Topology," IEEE/RSJ International Conference on Intelligent Robots and Systems (IROS 2000), Takamatsu, Japan, Oct. 31–Nov. 5, pp. 197–202.
- [8] Hirai, S., Masui, T., and Kawamura, S., 2001, "Prototyping Pneumatic Group Actuators Composed of Multiple Single-Motion Elastic Tubes," IEEE International Conference on Robotics and Automation (2001 ICRA), Seoul, South Korea, May 21–26, pp. 3807–3812.
- [9] Suzumori, K., Iikura, S., and Tanaka, H., 1991, "Development of Flexible Microactuator and Its Applications to Robotic Mechanisms," IEEE International Conference on Robotics and Automation (ICRA), Sacramento, CA, Apr. 9–11, pp. 1622–1627.
- [10] Martinez, R. V., Branch, J. L., Fish, C. R., Jin, L., Shepherd, R. F., Nunes, R. M. D., Suo, Z., and Whitesides, G. M., 2013, "Robotic Tentacles With Three-Dimensional Mobility Based on Flexible Elastomers," *Adv. Mater.*, **25**(2), pp. 205–212.
- [11] Merlet, J.-P., 2006, *Parallel Robots*, 2nd ed., Springer, Dordrecht, The Netherlands.
- [12] Bothema, R., and Roth, B., 1990, *Theoretical Kinematics*, Dover, New York.
- [13] Hopkins, J. B., and Culpepper, M. L., 2010, "Synthesis of Multi-Degree of Freedom, Parallel Flexure System Concepts Via Freedom and Constraint Topology (FACT)—Part I: Principles," *Precis. Eng.*, **34**(2), pp. 259–270.
- [14] Hopkins, J. B., 2007, "Design of Parallel Flexure Systems Via Freedom and Constraint Topologies (FACT)," Master's thesis, Massachusetts Institute of Technology, Cambridge, MA.
- [15] Ball, R. S., 1900, *A Treatise on the Theory of Screws*, The University Press, Cambridge, UK.
- [16] Phillips, J., 1984, *Freedom in Machinery: Volume I, Introducing Screw Theory*, Cambridge University Press, New York.
- [17] Hopkins, J. B., 2010, "Design of Flexure-Based Motion Stages for Mechatronic Systems Via Freedom, Actuation and Constraint Topologies (FACT)," Ph.D. thesis, Massachusetts Institute of Technology, Cambridge, MA.
- [18] Hopkins, J. B., and Culpepper, M. L., 2010, "A Screw Theory Basis for Quantitative and Graphical Design Tools That Define Layout of Actuators to Minimize Parasitic Errors in Parallel Flexure Systems," *Precis. Eng.*, **34**(4), pp. 767–776.
- [19] Su, H.-J., Hongliang, S., and Yu, J. J., 2012, "A Symbolic Formulation for Analytical Compliance Analysis and Synthesis of Flexure Mechanisms," *ASME J. Mech. Des.*, **134**(5), p. 051009.
- [20] Stewart, D., 1965, "A Platform With Six Degrees of Freedom," *Proc. Inst. Mech. Eng.*, **180**(1), pp. 371–386.
- [21] Uicker, J. J., Pennock, G. R., and Shigley, J. E., 2011, *Theory of Machines and Mechanisms*, 4th ed., Oxford University Press, New York.